Metals & corrosion

Synthesis, characterization and amorphization of mechanically alloyed $Fe_{75}Si_{12}Ti_6B_7$ and $Fe_{73}Si_{15}Ti_5B_7$ powders

A. Chebli[1,2,*] , Martin Cesnek[3], A. Djekoun[1], J. J. Sunol[4], and D. Niznansky[5]

[1] *Laboratory of Magnetism and Spectroscopy of Solids (LM2S), Faculty of Science, University of Badji-Mokhtar, B. P 12, 23000 Annaba, Algeria*

[2] *Higher School of Technological Education, Skikda, Algeria*

[3] *Department of Nuclear Reactors, Czech Technical University in Prague, V Holesovickach, 218000 Prague, Czech Republic*

[4] *Departamento de Física, Universitat de-Girona, Campus Montilivi, 17071 Girona, Spain*

[5] *Department of Inorganic Chemistry Charles, Faculty of Science, University in Prague, Hlavova8, 128-42, Praha 2, Czech Republic*

ABSTRACT

In this study, $Fe_{75}Si_{12}Ti_6B_7$ and $Fe_{73}Si_{15}Ti_5B_7$ (wt. %) alloy powders were synthesized from pure elemental powders by a mechanical alloying (MA) method under argon atmosphere. The evolution in particles morphology, chemical composition, crystalline structure, magnetic and hyperfine proprieties of the mixture elements during MA(0–80 h) was investigated by scanning electron microscopy attached with energy-dispersive spectroscopy, X-ray diffraction (XRD), vibrating sample magnetometer and Mössbauer spectroscopy (MS). The Rietveld refinement of the XRD pattern of the samples milled 5 h shows the formation of several structures: Fe_3Si, α-Fe nanostructured, Fe_2Ti and Fe_2B, in addition, that the structure became much more amorphous together with increasing milling time at 80 h. The thermal stability of powders milled was characterized by differential scanning calorimetry (DSC). The annealing of samples milled 80 h shows that the crystallization of the amorphous phases and the activation energy determined by using Kissinger's equation was 462.23 ± 16.11 kJ mol^{-1} and 798.43 ± 16.12 kJ mol^{-1} for the $Fe_{73}Si_{15}Ti_5B_7$ and $Fe_{75}Si_{12}Ti_6B_7$, respectively. Moreover, the results from XRD and DSC for 80 h of milling were approved by the Mössbauer spectroscopy, and the spectra revealed that the sample $Fe_{73}Si_{15}Ti_5B_7$ is fully amorphous, but the sample $Fe_{75}Si_{12}Ti_6B_7$ still contains some of Fe with a 2.8% fraction non- detected by XRD. The saturation magnetization (Ms) and coercivity values were of about 151 emu/g, 38.5

https://doi.org/10.1007/s10853-022-07404-4

G for $Fe_{73}Si_{15}Ti_5B_7$ and 171.6 emu/g, 35 G for $Fe_{75}Si_{12}Ti_6B_7$, respectively, after 80 h of milling.

Introduction

Fe-based amorphous materials have received a great attention owing to the fact that they possess various and excellent properties, including high degradation ability, high efficiency, stability, reusability in addition to the excellent corrosive–wear resistant, wide adaptability [1, 2] and soft magnetic properties [3, 4]. These materials can be widely used in industrial manufacturers, like transformers, magnetic recording heads, converters, magnetic media and permanent magnets [5–9]. Several methods have been used to elaborate Fe-based amorphous alloys including, rapid solidification [10, 11], induction melting technique [12], melt-spinning technique[13], laser cladding [14] and mechanical allowing [15, 16], and among which, the mechanical alloying (MA) process is the common used technique. This is because they exhibit relatively low-cost equipment, simplicity, moderate-temperature processing and the power to produce large quantities of homogeneous materials. Nevertheless, the MA process is sensible to the contamination by the milling tools affecting some properties of amorphous powder, such as thermal stability and chemical composition.

Many studies have been carried on where MA has been successfully applied to produce Fe-based binary, ternary or multi-component alloys amorphous. Additionally, the effects of metal elements (Cr, Ni, Al, Cu, Nb, B, Mo, Ti and Mn) on the properties of the Fe–Si alloy have been reported in previous studies showing significant changes in structural properties, mechanical, magnetic and thermal [17–27]. In this regard, K. M. Agrawal et al. [17] found that Mn increases the amorphization rate, as well as the high fraction of Cu provides good manufacturability in FeSiBi alloys, and aluminum increases the corrosion resistance. However, Ti decreases the electrochemical corrosion performance, and the small amount of Cr significantly improves the corrosion resistance of the FeSiB amorphous alloys.

In the present work, the $Fe_{75}Si_{12}Ti_6B_7$ and $Fe_{73}Si_{15}Ti_5B_7$ (wt. %) alloy powder, was elaborated by mechanical alloying, whose objective is to develop an alloy of good amorphous-phase stability for application as a soft magnetic material.

The morphological, chemical, structural, thermal and magnetic characterization at different milling times was performed by, XRD, SEM, VSM, SM and DSC.

Production of samples

Quaternary alloys $Fe_{75}Si_{12}Ti_6B_7$ (wt. %) and $Fe_{73}Si_{15}Ti_5B_7$ (wt. %) were prepared from high-purity elemental powders; silicon (Si, 99.9%, average particle size < 30 μm), iron (Fe, 99.98%, average particle size < 30 μm), titanium (Ti, 99.7%, average particle size < 15 μm) and boron (B, amorphous structure, 99.7%, average particle size < 30 μm). Mechanical alloying (MA) process was performed in a high-energy planetary ball mill (Fritsch P7) under argon atmosphere using six balls and two steel vial with the ball-to-powder weight ratio (BPR) as 20:1, the rotation speed of the vials as 500 rpm, and the milling times ranged from 5 h up to 80 h. To avoid excessive heating during the milling process, a break time of ¼ h was applied after each ½ h of MA process. For each milling times, 1 ml of benzene (C_6H_6) was added inside the vial and used as the process control agent (PCA). Hence, the objective of this operation is to prevent excessive cold welding of the powders, to eliminate adherence of the powders to the vial and to obtain important quantity of powders. The powders were collected under argon atmosphere.

Further, the particle morphology of powders was examined by scanning electron microscopy coupled with energy-dispersive X-ray spectroscopy (SEM/EDX) using DSM 960A ZEISS microscope. The samples structure was characterized by X-ray diffraction (XRD) using the Cuk_α radiation ($\lambda = 0.154056$ nm) in 2θ range 10–120° with step size of $2\theta = 0.02^\circ$, since the identification of phases structural parameters was provided from the Rietveld refinement of the XRD patterns using the MAUD program [28]. In addition, the differential scanning calorimetry (DSC) method in the range 30–1000 °C at a heating rate of 10 $^\circ$C/min

under argon atmosphere was used to examine the thermal stability of the alloys.

The magnetic characterizations were carried out using vibrating sample magnetometer (VSM) at room temperature within an external field up to 10,000 G. Mössbauer spectra were recorded at room temperature (RT) using constant acceleration spectrometer with ^{57}Co/Rh gamma ray source. The resulting isomer shifts are given relative to the MS spectrum of α-Fe recorded at RT. The spectral parameters comprising isomer shift (IS), quadrupole shift/quadrupole splitting (QS), hyperfine magnetic field (B), line width (Γ) and area (A) of spectral components were refined by the CONFIT [29] curve-fitting program.

Results and discussion

Morphological study

Figure 1 shows the evolution of the powders morphology during the MA process. The un-milled powders have random size, and different shapes and sizes, as well as some particles having a heterogeneous spherical shape are likely iron particles.

After 5 h of milling, a significant change was noticed in the morphology of the powder particles, and hence, during milling process, the powders are alternately welded and fractured, and at this step of milling, can be seen clearly the homogeneity of the particles shape and the lamellar structure or the flattened shape.

After 20 h of milling, the particles with more uniform sizes and some agglomeration ones are observed. Up to 40 h of milling, the morphology of the majority of particles became small and homogeneity of shapes of the particles is visible, this is due to reason that in this step of milling, the fracture mechanism becomes dominant. We also refer to the emergence of spherical shapes, accordingly to that reported [30–34], proving the appearance of the spherical shape signifies the formation of solid-state amorphization. With increasing milling time at 80 h, the particles became smaller and identical shape. Therefore, the equilibrium between fracturing and cold welding leads to the homogeneity of particles shape.

Figure 2 depicts the EDS pattern analysis of the two samples for 0, 40 and 80 h, the Fe, Si and Ti were detected. The boron is not observed because is in

amorphous state. In fact, the EDS analysis showed the presence of small quantities of several chemical elements, including Cr, Ni, O and carbon (Table 1), indicating the contamination of samples from the atmosphere and the milling tools. This contamination is likely incorporated in the lattice and alters the crystal periodicity.

Structure evolution during MA

The shocks repeated during high-energy milling process create severe plastic deformations, leading consequently to produce various defects in the crystal lattices, dislocations, vacancies and interstitials which are the origin for a solid-state reaction to occur.

The structural changes of the samples during MA are evinced by the evolution of the XRD patterns.

Figure 3a, b shows the XRD patterns of the $Fe_{75}Si_{12}Ti_6B_7$ and $Fe_{73}Si_{15}Ti_5B_7$ samples for different milling times. The XRD pattern of un-milled powder mixture (0 h) displayed all the peaks of the constituent mixture elements α-Fe (ICDD Card No: 87–0721, cubic, Im-3ma), Si (ICDD Card No. 27-1402, face-centered cubic (fcc), Fd-3 m) and Ti (ICDD Card No. 44-1294, hexagonal, P63/mmc), except B element which is in amorphous state [35] (Fig. 4).

The milling of the initial elements leads to a decrease in the intensity and the broadening in diffraction peaks attributing to the grain size reduction and an increase in the microstrain, in addition to the disappearance and appearance of new diffraction peaks explaining formation of new phases.

After 5 h of milling, the all Ti and Si Bragg peaks diffraction disappear, and a broad lines diffraction appeared at 2θ ≈ 44.55°, 65.11°, 82.15°, 98.78° and 116.25° corresponding to iron α-Fe. At this initial milling step, the α-Fe nano-crystallites east formatted, and the disappearance of diffraction lings corresponding to Ti and Si elements can be related to the start of inter-diffusion between mixture elements and formation of the new phases. The best Rietveld refinement of the 5 h milled pattern for two compositions $Fe_{75}Si_{12}Ti_6B_7$ and $Fe_{73}Si_{15}Ti_5B_7$ (Fig. 5a, b) is executed with several phases, including α-Fe nanostructured, Fe_3Si (FCC structure), Fe_2Ti and Fe_2B (tetragonal crystal structure). In this context, Wang et al. [36] reported the formation of an amorphous phase and crystallization phases of Fe_3Si, Fe_2P of Fe–Cr–Si–P alloy and the coating having a high hardness, wear resistance and corrosion resistance. In addition, D.D.
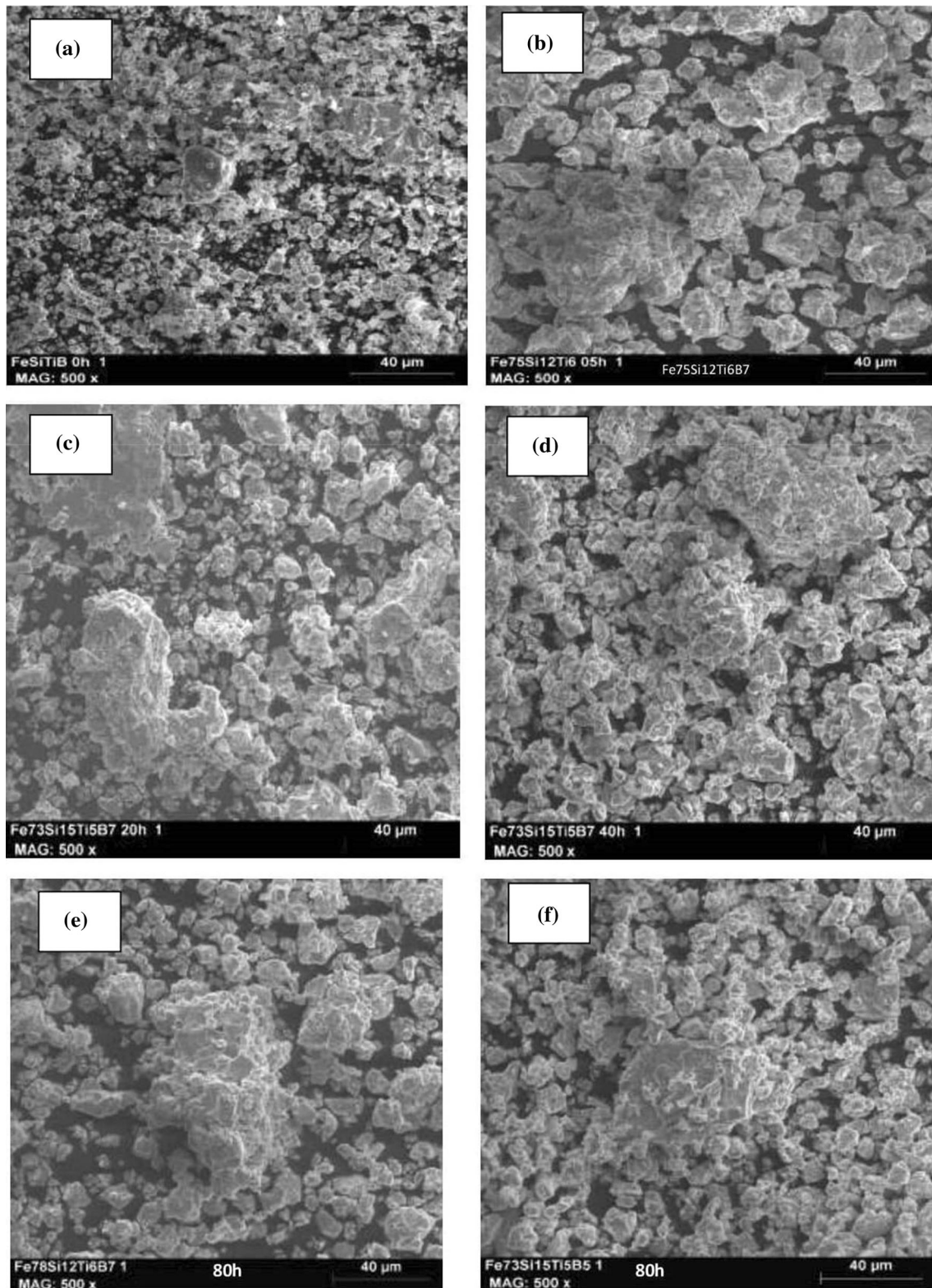
Figure 1 Scanning electron micrographs (SEM) of samples at various milling times: **a** 0 h, **b** 5 h, **c** 20 h, **d** 40 h and **e f** 80 h.

Xu et al. [20] found that the coexistence of the two phases Fe_3B and Fe_3Si for $Fe_{76.5}Si_{9.5}B_{11}Cr_3$ amorphous alloys and amount of Cr can increase the glass-forming ability.
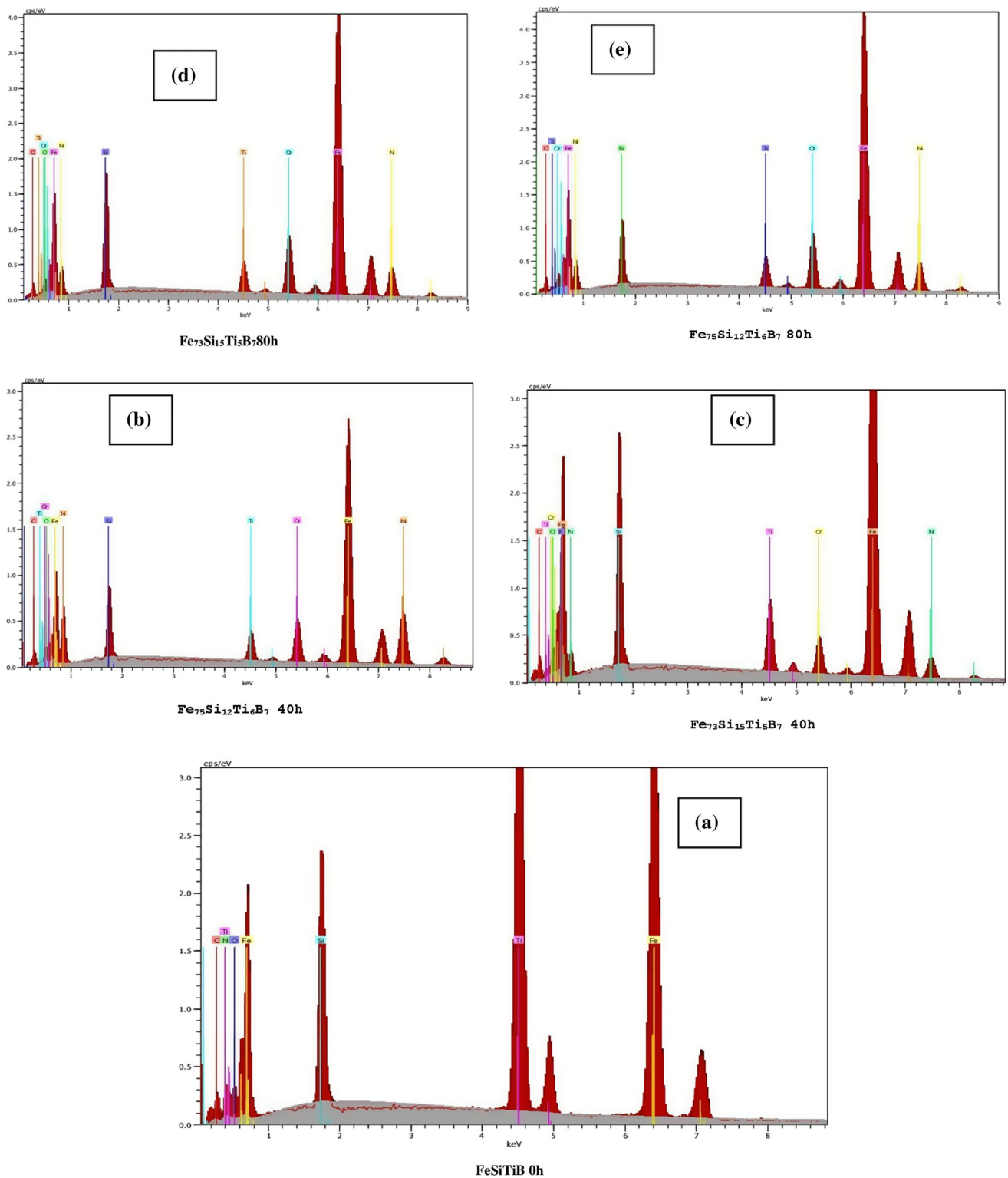
Figure 2 EDS of $Fe_{75}Si_{12}Ti_6B_7$ and $Fe_{73}Si_{15}Ti_5B_7$ samples for **a** 0 h, **b** and **c** 40 h and **d** and **e** 80 h.

Table 1 Atomic proportion composition from EDS analysis of the $Fe_{73}Si_{15}Ti_5B_7$ and $Fe_{75}Si_{12}Ti_6B_7$ milled for 0, 40 and 80 h

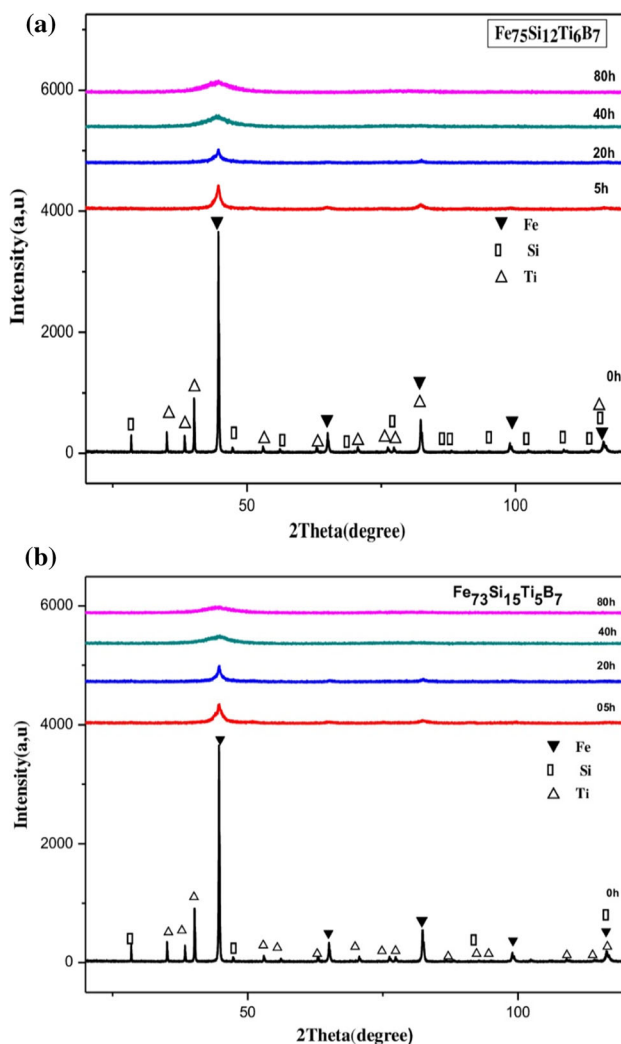| Elements/samples (wt.%)	FeSiTiB	$Fe_{73}Si_{15}Ti_5B_7$(40 h)	$Fe_{75}Si_{12}Ti_6B_7$(40 h)	$Fe_{73}Si_{15}Ti_5B_7$(80 h)	$Fe_{75}Si_{12}Ti_6B_7$(80 h)
Iron	54.03	69.42	57.12	64.89	67.13
Silicon	5.76	7.85	4.28	6.17	3.79
Titanium	30.79	5.08	3.63	3.35	3.67
Oxygen	4.71	2.24	1.95	1.55	
Nitrogen	0.00	0.89			
Carbon	6.02	6.82	6.96	6.36	6.81
Nickel		4.75	20.05	10.32	11.05
Chromium		2.95	6.01	7.37	7.56
Fluorine		0.89			

Figure 3 a XRD patterns of $Fe_{75}Si_{12}B_6Ti_7$ samples at different milling time. b XRD patterns of $Fe_{73}Si_{15}Ti_5B_7$ samples as a function of milling time.

After 20 h of milling, a strong reduction in intensity and a significant broadened of the peaks are
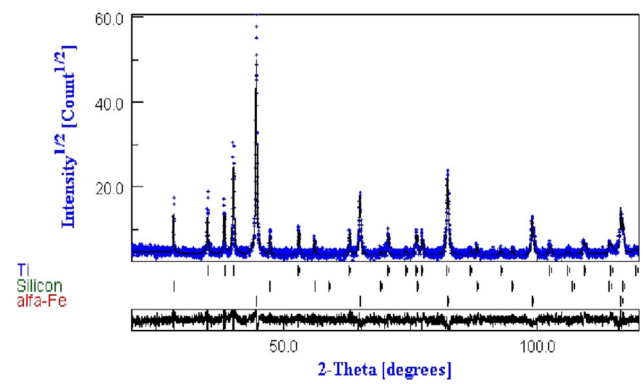

Figure 4 Rietveld refinement of the XRD pattern of un-milled powders FeSiBTi. Experimental (dots) and calculated (full line) patterns are shown. Difference is given below (GOF = 1.13).

observed. Moreover, the XRD pattern is composed of well defined Bragg peaks and a diffuse halo around $2\theta \approx 44.55°$. The latter is typical of the amorphous phase; in addition, the increase in the base line was assigned to the non-coherent diffraction domains, as the characteristics of grain boundaries, which exhibit an amorphous-like phase [37]. By progression of milling time, the patterns for 40 h and 80 h contain only broad peak at $2\theta \approx 44.5°$, without any Bragg peak showing traces of crystallites, indicating the amorphization of the samples.

The production of amorphous material by mechanical alloying can be explained by the large amount of defects introduced in the powders during milling and simultaneously during reduction of the particles size to about few nanometers. However, the high-energy milling process destroys the crystallites phase by creation of various defects linear and punctual and also leads to the increase in the grain-boundaries amount characterized by disorder atomic arrangement. In addition to the milling advantages,
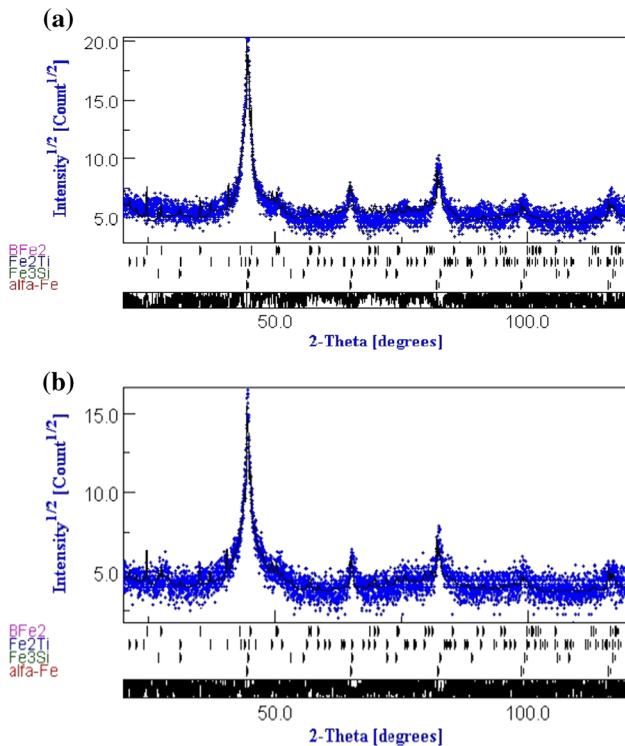
(a)

(b)

Figure 5 **b** Rietveld refinement of the XRD pattern of powders $Fe_{73}Si_{15}B_5Ti_7$ milled for 5 h. Experimental (dots) and calculated (full line) patterns are shown. Difference is given below (GOF = 1.13).

the nature of the chemical elements, such as silicon and boron, belongs to elements favoring the amorphization of Fe-based alloys [38, 39]. Different Fe-based amorphous have been obtained by high-energy mechanical allowing, for example FeMoPCB [40], $Fe_{32.5}Co_{32.5}Nb_{35}$ [41], FeSiBAlNi(Nb) [42], AlFe-CuZnTi [43], $Fe_{26.7}Co_{28.5}Ni_{28.5}Si_{4.6}B_{8.7}P_3$ [44] and FeSiBAlNi [45]. As usual, the progression of the MA process leads to the increase in the quantity and homogeneity of the amorphous phase.

Thermal analysis and activation energy

To study the thermal stability of the powders milled at different times, the DSC measurement was performed from 30 to 700 °C.

Figure 6 shows the DSC curves of the two samples for 0, 5, 20, 40 and 80 h of milling times taken at heating rate of 10 °C/min. For the powders un-milled, we observed a single wide peak similar to bump ranging from 550 to 650 °C which is probably due to the structural relaxation during the samples heating.

For samples milled 5 h, the DSC curve consisting a broad exothermic peak at the 490.02 °C and at the 593 °C, corresponding most probably to the formation of the Fe_2Ti, Fe_3Si and Fe_2B phases. The presence of these phases in the samples subjected to the DSC measurements was detected by XRD. Similar results were proved in Fe–Si–B amorphous alloys elaborated by melt spinning [46].

The curves (DSC) for samples milled at 20, 40 and 80 h except the sample $Fe_{73}Si_{15}Ti5B_7$ milled at 20 h are identical and represent exothermic peak at temperature ranging from 550 to 585 °C. As reported [47], this exothermic reaction is associated with the crystallization of amorphous alloy. However, the increased milling time leads to appear less wide and more intense crystallization peak (Fig. 7), indicating an increase in the volume fraction of the amorphous phase, and accordingly a similar exothermic reaction has been previously obtained on some Fe-based amorphous alloys containing Si [20, 31, 48–68].

The thermal analysis method (DSC) was developed to study crystallization phenomena in amorphous alloys. Overall, crystallization kinetics are often elucidated in terms of the standard nucleation growth model [52]. The activation energy (E_a) for crystallization is a decisive kinetic parameter for thermal stability of the amorphous phase, and the activation energy is associated with the growth process of peak the crystallization. Based on the results of the exothermic peak shifts in DSC measurements conducted at different heating rates, the value of the apparent activation energy for thermal crystallization can be determined.

The DSC curves with various heating rates (5, 10, 20 and 40 °C/min) are exhibited in Fig. 8 for the samples of $Fe_{75}Si_{12}Ti_6B_7$ and $Fe_{73}Si_{15}Ti_5B_7$ milled 80 h, respectively. All the DSC scans represent one exothermic peak, which is characteristic of the crystallization peak temperature (Tc).

For both samples, the exothermic peaks for crystallization shift to lower temperature at lower heating rates. According to Kissinger analysis investigating the crystallization of amorphous alloys, the apparent activation energy (E_a) for crystallization process can be determined by the following relation [53]:

$$\ln\left(\frac{\beta}{T_c^2}\right) = -\frac{E_a}{RT_c} + c, \tag{1}$$

where R = 8,315 J/K is the gas constant, β is the heating rate, c is the constant and T_c is the peak

Figure 6 Curves DSC of $Fe_{73}Si_{15}B_5Ti_7$ and $Fe_{75}Si_{12}B_6Ti_7$ samples at different milling time.
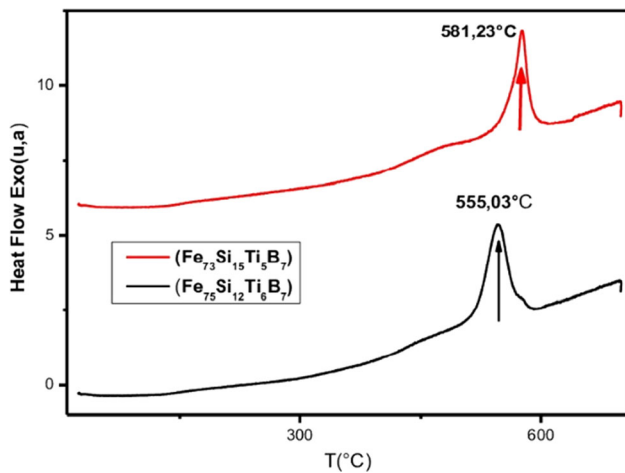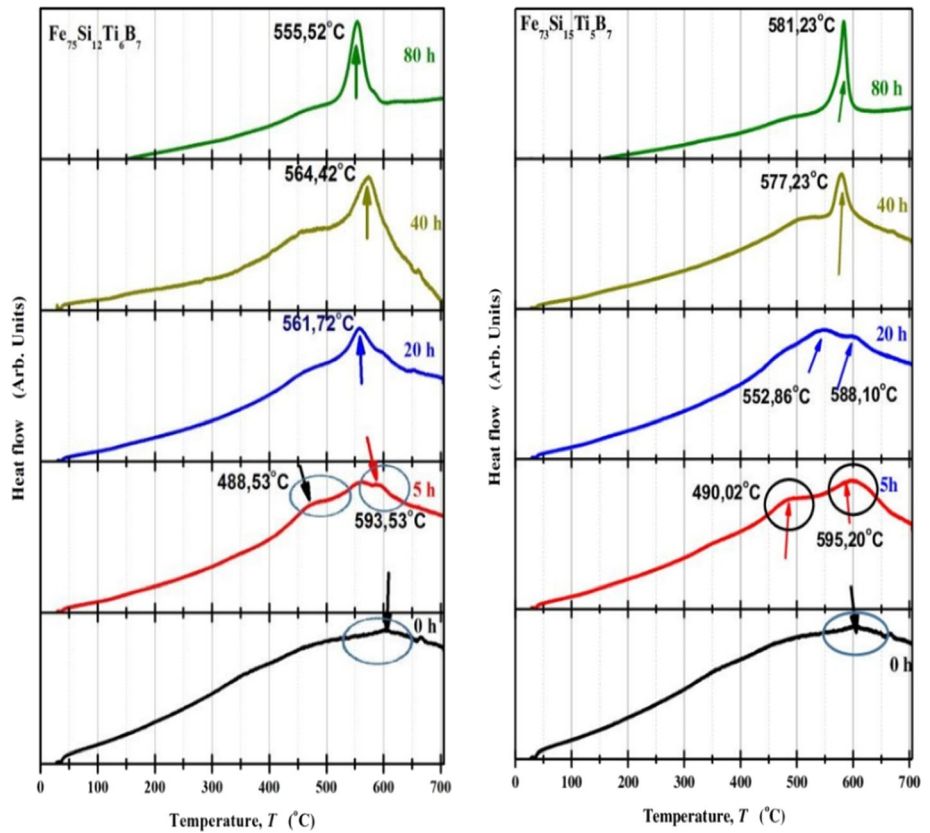
Figure 7 Curves DSC of $Fe_{73}Si_{15}B_5Ti_7$ and $Fe_{75}Si_{12}B_6Ti_7$ samples after 80 h of milling.

temperature of the amorphous crystallization for each rate. A straight line was approximately obtained by plotting $\ln\left(\frac{\beta}{T_c^2}\right)$ versus $\frac{1}{T_c}$ as shown in Fig. 9a, b. From the slope of the line, the activation energy was calculated and found to be 462.23 ± 16.11 kJ mol^{-1} and 798.43 ± 16.12 kJ mol^{-1} for the $Fe_{73}Si_{15}Ti_5B_7$ and $Fe_{75}Si_{12}Ti_6B_7$, respectively. The activation energy for

pure Iron was found as 174 kJ mol^{-1} and 282 kJ mol^{-1} for grain boundary diffusion and of lattice diffusion, respectively [54]. The addition of other elements to Fe-based alloy may increase or decrease this value, and the activation energy increases with Fe content. Similar results were evolved for FeSiBP and FeCoSiBP [55], FeNiPSi [56], $Fe_{100-x}(NbTiTa)_x$ ($x = 20$, 30 and 40) [57] and $Co_{40-}Fe_{22}Ta_8B_{30}$ [31] amorphous materials. As reported by Liu et al. [58], (Ea) is mightily reliant on the ratio of amorphous phase and is appreciably decrease with grow of volume proportion of the nanostructured phases in the amorphous matrix.

Magnetic behavior

The magnetic properties of samples were studied by vibrating sample magnetometer (VSM). A hysteresis curve of the 0, 5, 20, 40 and 80 h milled $Fe_{75}Si_{12}Ti_6B_7$ and $Fe_{73}Si_{15}Ti_5B_7$ alloy powder was plotted by magnetization (M) versus applied magnetic field (H) (Fig. 10a, b). These curves present a sigmoidal form, typically of nanostructured alloys with small magnetic domains. The soft magnetic alloys are characterized by low coercivity and the important

Figure 8 DSC spectra of the Fe$_{73}$Si$_{15}$B$_5$Ti$_7$ and Fe$_{75}$Si$_{12}$B$_6$Ti$_7$ sample milled for 80 h as a function of heating rate 5 min°C^{-1}, 10 min°C^{-1}, 20 min°C^{-1} and 40 min°C^{-1}.
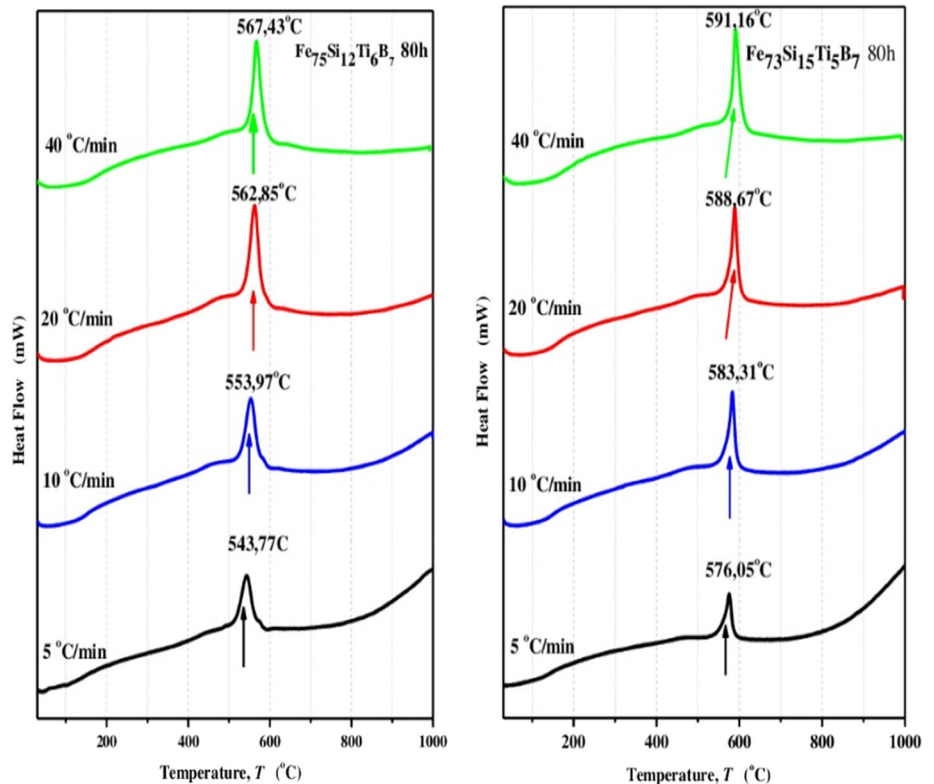
characteristics desired for all soft magnetic applications are the low coercivity, high saturation induction and high permeability [59].

The magnetization (Ms) coercivity (Hs) and the remanence to saturation ratio Mr/Ms were determined from these hysteresis curves.

Figure 11a, b displays the variation of Ms and Hc for different milling times for two samples Fe$_{75}$Si$_{12}$Ti$_6$B$_7$ and Fe$_{73}$Si$_{15}$Ti$_5$B$_7$. Two steps can be observed; the Ms rapidly decreasing from 249 to 105 emu/g for the composition Fe$_{73}$Si$_{15}$Ti$_5$B$_7$ for 0–20 h of milling, and from 249 to 152 emu/g for 0–5 h of milling for Fe$_{75}$Si$_{12}$Ti$_6$B$_7$, then the increasing in Ms at values of 151 and 171.6 emu/g after 80 h of milling for Fe$_{75}$Si$_{12}$Ti$_6$B$_7$ and Fe$_{73}$Si$_{15}$Ti$_5$B$_7$, respectively. As previously reported [60, 61], the decrease in Ms is mainly due to the early interaction between the ferromagnetic Fe atoms with the non-ferromagnetic, Si, B and Ti atoms. The dissolution of non-ferromagnetic or paramagnetic atoms into the microstructure of the powders can reduce the density of magnetic atom interaction, and the formation of amorphous phase

leads to a decrease in the Ms [62]. Of note, the Ms of α-Fe nanoparticles was about to190 emu/g [63].

As can be seen, the Hc increases from 31 to 130 G and to 165 G for Fe$_{75}$Si$_{12}$Ti$_6$B$_7$ and Fe$_{73}$Si$_{15}$Ti$_5$B$_7$, respectively, then decreases and reaches a value of 38.5 G and 35 G after 80 h of milling for Fe$_{75}$Si$_{12}$Ti$_6$B$_7$ and Fe$_{73}$Si$_{15}$Ti$_5$B$_7$. The increase in Hc in the early step of milling could be associated with the plastic deformation effect and different of defects and shape form of the particles [64, 65]. The decrease in Hc might be due to the formation of amorphous phase and the effect of milling on particle size during the MA.

Figure 12a and b exhibits the variation of the magnetic ratio (Mr/Ms) for various milling time. The Mr/Ms evolution is similar to coercivity changes, increased in the first step of milling (0–5 h), then decreased continuously by increasing milling time.

Spectrometry Mössbauer

Mössbauer spectra were recorded at room temperature (RT) using constant acceleration spectrometer
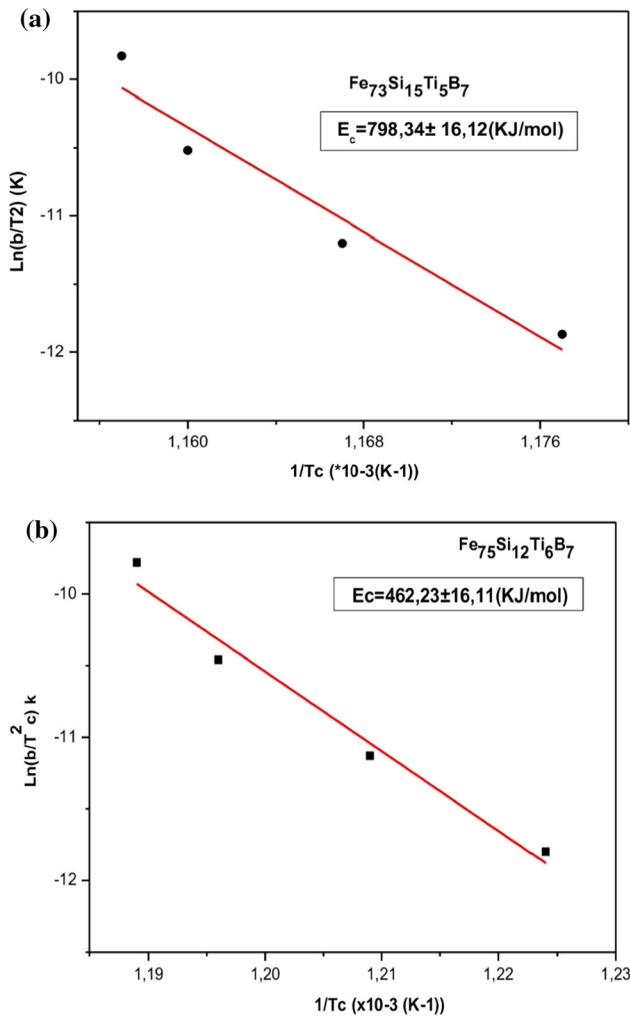
Figure 9 a Kissinger plots of $\ln(\beta/T_c^2)$ versus $\frac{1}{T_c}$ for the crystallization in $Fe_{73}Si_{15}B_5Ti_7$ powder. **b** Kissinger plots of $\ln(\beta/T_c^2)$ versus $\frac{1}{T_c}$ for the crystallization in $Fe_{75}Si_{12}B_6Ti_7$ powder.

with $^{57}Co/Rh$ gamma ray source. The resulting isomer shifts are given to be relative to the MS spectrum of α-Fe recorded at RT. The spectral parameters comprising isomer shift (IS), quadrupole shift/ quadrupole splitting (QS), hyperfine magnetic field (B), line width (Γ) and area (A) of spectral components were refined by the CONFIT curve-fitting program [28].

Figure 13 displays the MS spectrum of the unmilled powder ($Fe_{73}Si_{15}Ti_5B_7$), showing sextet with hyperfine parameters (IS = 0.00 ± 0.02 mm/s, QS = 0.00 ± 0.02 mm/s, B = 33.0 ± 0.5 T) identical with hyperfine parameters of α-Fe obtained at RT.
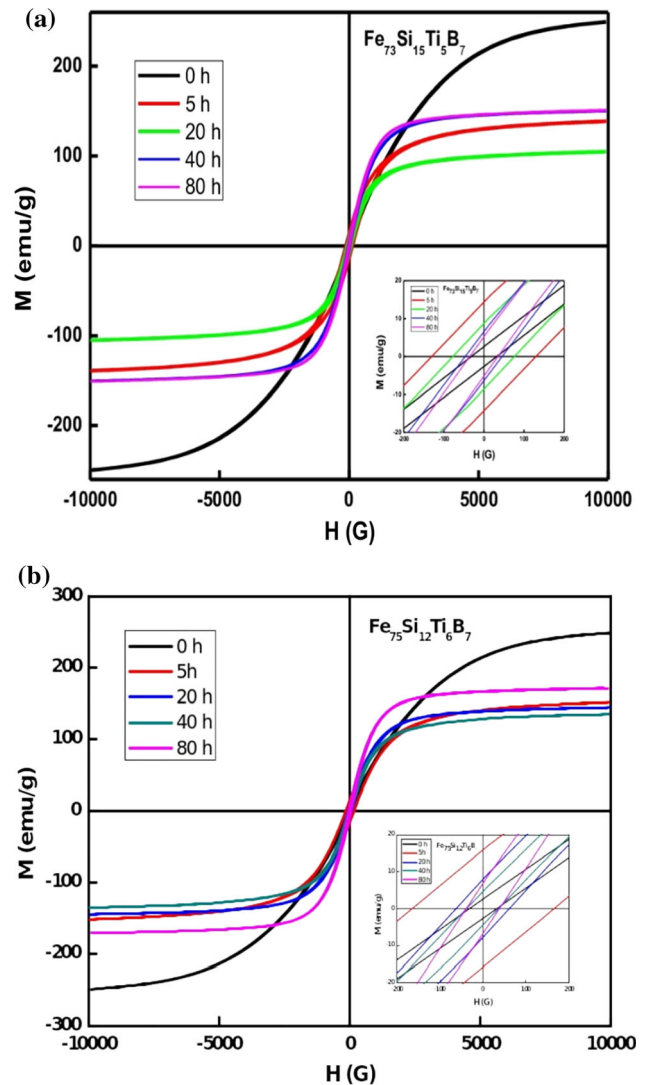
Figure 10 a Hysteresis loop of $Fe_{73}Si_{15}B_5Ti_7$ samples with different milling time. **b** Hysteresis loop of $Fe_{75}Si_{12}B_6Ti_7$ samples with different milling time.

MS spectra of the $Fe_{73}Si_{15}Ti_5B_7$ sample after different periods (5, 20 and 40 h) of milling process are shown in Fig. 14 together with the corresponding distributions of hyperfine magnetic field P (B). Obviously, the milling process triggered structural changes. All the spectra after milling process are a combination of sextet with relatively narrow lines characteristic for crystalline phase and relatively broad sextets characterizing the amorphous materials. Hyperfine parameters of spectral components are listed in Table 2. Sharp sextet S1 corresponds to α-Fe
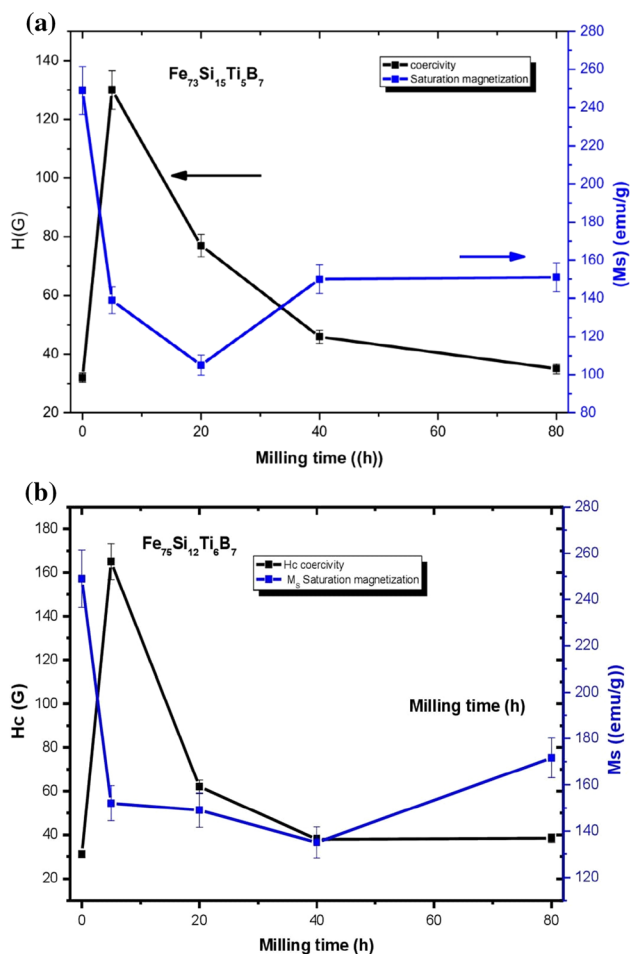
Figure 11 **a** Coercivity (Hc) and saturation magnetization (Ms) as a function of milling time for $Fe_{73}Si_{15}B_5Ti_7$ sample. **b** Coercivity (Hc) and saturation magnetization (Ms) as a function of milling time for $Fe_{75}Si_{12}B_6Ti_7$ sample.

Figure 12 **a** The ratio (Mr/Ms) for $Fe_{75}Si_{12}B_6Ti_7$ sample at different milling time. **b** The ratio (Mr/Ms) for $Fe_{75}Si_{12}B_6Ti_7$ sample at different milling time.

phase. Furthermore, broadened character of sextet S2 exhibiting hyperfine field ∼ 30 T suggests some level of structural disordering. It might represent some state between crystalline and fully disordered state of the sample. The rest of the spectra correspond to amorphous part and is fitted by distributions of hyperfine magnetic field. It can be seen that the contribution of α-Fe to overall spectra decreases with increasing milling time while the contribution of amorphous part increases. In addition, the changes of distribution of hyperfine magnetic field with increasing milling time have been noticed. After 5 h of milling, the distribution of hyperfine magnetic
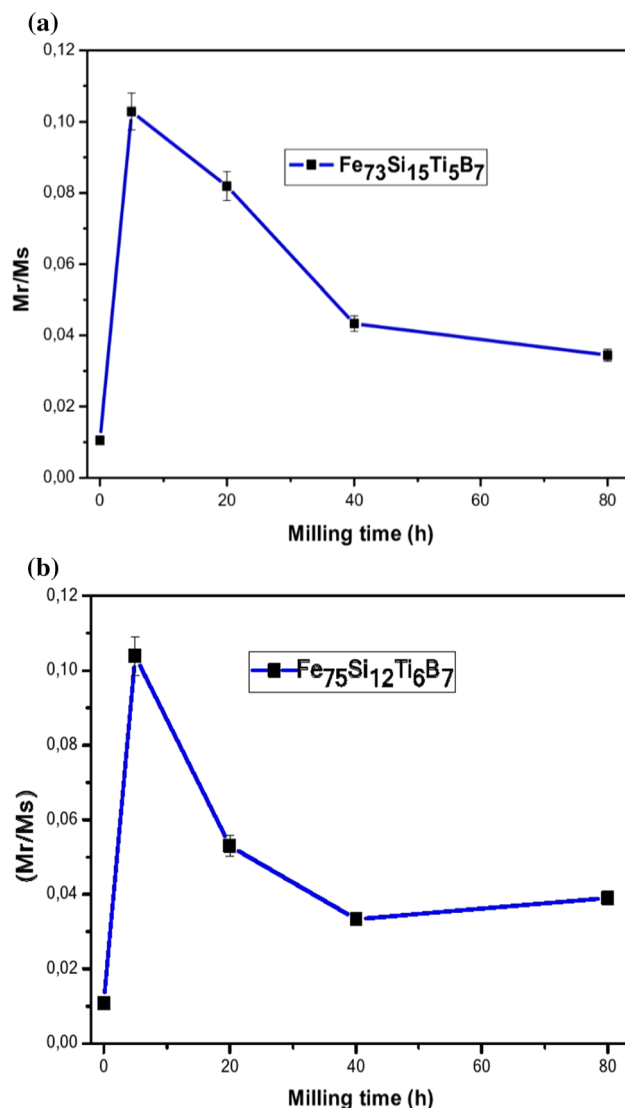
field covers relatively broad range of *B*-values. With increasing milling time, the distribution of hyperfine magnetic field becomes narrower, and after 40 h, two well distinguishable lower and higher hyperfine magnetic regions can be observed. It can be also noticed that the mean value of hyperfine magnetic field of the amorphous part decreased from ∼ 15 T to ∼ 11 T after milling for 20 h. However, after 40 h the mean value of hyperfine magnetic field increased
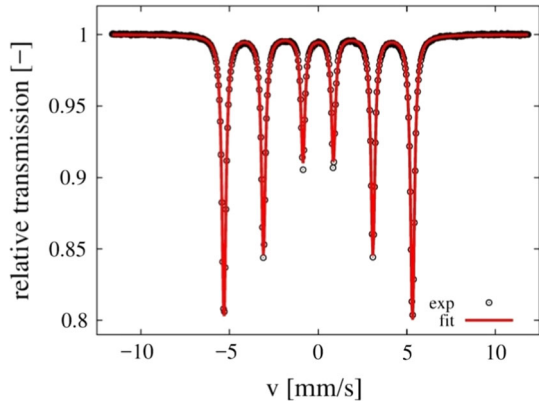
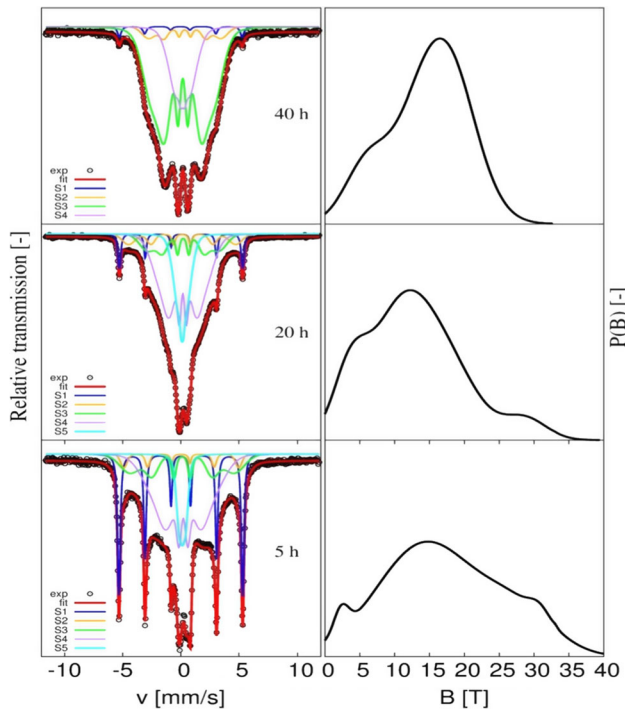**Figure 13** MS spectrum of the FeSiBTi sample un-milled recorded at RT.

Figure 14 MS spectra of the sample with nominal chemical composition $Fe_{73}Si_{15}Ti_5B_7$ after indicated period of milling recorded at room temperature..

again to ∼ 14 T. The mean value of IS of amorphous part changes only within the error.

For powders milled at 80 h, the sample $Fe_{73}Si_{15}Ti_5B_7$ is fully amorphous with < Bhf > = 11.3 ± 0.5 T and < IS > 0.14 ± 0.02 mm/s (Fig. 15), while the

second sample with chemical composition $Fe_{75}Si_{12}Ti_6B_7$ still contains phase with parameters almost equal to alpha-Fe (Bhf = 33.0 T, QS = 0.06 mm/s, IS = -0.02 mm/s) with area fraction A = 2.8% (Fig. 16). Parameters of the amorphous part are < Bhf > = 4.7 ± 0.5 T and < IS > 0.16 ± 0.02 mm/s.

In addition, the difference between the XRD and SM results may be originated from the quite small of α-Fe phase, which cannot be detected by the XRD, especially for the phases proportion $x \leq 4$[66–68].

Conclusion

Amorphous $Fe_{73}Si_{15}Ti_5B_7$ and $Fe_{75}Si_{12}Ti_6B_7$ (wt %) alloys were successfully obtained by mechanical alloying from elemental powder mixture of iron, silicon, titanium and boron.

The Rietveld refinement of XRD pattern of samples milled 5 h reveals the formation of phases α-Fe nanostructured, Fe_3Si, Fe_2Ti and Fe_2B.

The increasing milling time for 80 h makes the amorphous phase become a dominant structure.

The DSC measurement results in the crystallization of the powder occur at about 550 − 585 °C. The activation energy was calculated and found to be 462.23 ± 16.11 kJ mol^{-1} and 798.43 ± 16.12 kJ mol^{-1} for the $Fe_{73}Si_{15}Ti_5B_7$ and $Fe_{75}Si_{12}Ti_6B_7$, respectively. The results indicate that the appropriate amounts of elements can significantly enhance the thermal stability of Fe-based alloys.

The magnetization values are about 151 and 171.6 emu/g after 80 h of milling for $Fe_{73}Si_{15}Ti_5B_7$ and $Fe_{75}Si_{12}Ti_6B_7$, respectively. It is an identical behavior like that of ferromagnetic materials. The Mössbauer spectroscopy approved the results found by XRD and DSC, however the MS shows that the sample $Fe_{73}Si_{15}Ti_5B_7$ milled at 80 h is fully amorphous, but the sample with chemical composition $Fe_{75}Si_{12}Ti_6B_7$ still contains phase with parameters almost equal to α-Fe (Bhf = 33.0 T, QS = 0.06 mm/s, IS = − 0.02 mm/s) with area fraction A = 2.8% not detected by XRD.

Table 2 Hyperfine parameters of spectral components. IS and B of amorphous parts are mean values

Milling time	Spectral component	A [%]	IS [mm/s] ± 0.02 mm/s	QS [mm/s] ± 0.02 mm/s	B [T] ± 0.5 T
5 h	S1	22.6	0.00	0.00	33.1
	S2	4.3	0.03	0.04	30.7
	Amorphous part (S3–S5)	73.1	0.18	–	15.8
20 h	S1	7.3	0.01	0.00	33.0
	S2	7.7	0.11	0.01	28.6
	Amorphous part (S3–S5)	85.0	0.17	–	11.0
40 h	S1	2.6	− 0.02	0.04	32.8
	Amorphous part (S2–S4)	97.4	0.19	–	14.0

Figure 15 MS spectrum of the sample $Fe_{75}Si_{12}Ti_6B_7$ milled for 80 h.
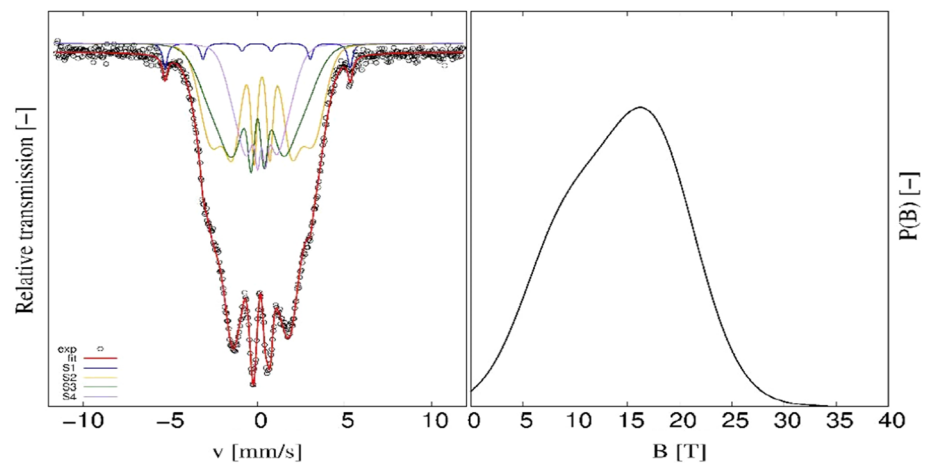
Figure 16 MS spectrum of the sample $Fe_{73.5}Si_{15}Ti_5B_7$ milled for 80 h.
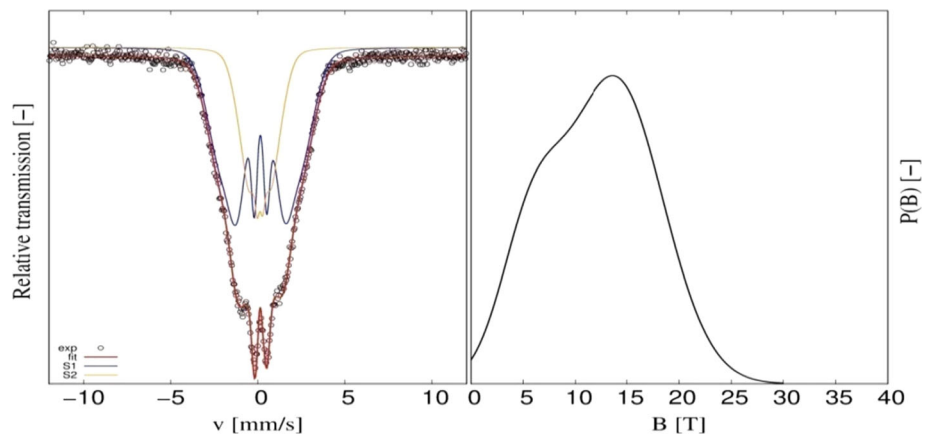
Declarations

Conflict of Interest The authors declare that they have no conflict of interest.

References

[1] Jia Z, Zhang WC, Wang WM, Habibi D, Zhang LC (2016) Amorphous $Fe_{78}Si_9B_{13}$ alloy: a rapid and reusable photo-enhanced Fenton-like catalyst in degradation of Cibacron Brilliant Red 3B-A dye under UV–vis light. Appl Catal B 192:46–56

[2] Tripathi MK, Chattopadhyay PP, Ganguly S (2015) Multi-variate analysis and classification of bulk metallic glasses using principal component analysis. Comput Mater Sci 107:79–87

[3] Suryanarayana C, Inoue A (2013) Iron-based bulk metallic glasses. Int Mater Rev 58:131–166

[4] Panigrahi M, Avar B (2021) Influence of mechanical alloying on structural, thermal, and magnetic properties of $Fe_{50-}Ni_{10}Co_{10}Ti_{10}B_{20}$ high entropy soft magnetic alloy. J Mater Sci Mater Electron 32:21124–21134

[5] Koga GY, Nogueira RP, Roche V, Yavari AR, Melle AK, Gallego J, Bolfarini C, Kiminami CS, Botta WJ (2014) Corrosion properties of Fe–Cr–Nb–B amorphous alloys and coatings. Surf Coat Technol 254:238–243

[6] Souza CAC, Ribeiro DV, Kiminami CS (2016) Corrosion resistance of Fe–Cr–based amorphous alloys: an overview. J Non-Cryst Solids 442:56–66

[7] Zheng HJ, Hu LN, Zhao X, Wang CZ, Sun QJ, Wang T, Hui XD, Yue YZ, Bian XF (2017) Poor glass–forming ability of Fe–based alloys: its origin in high-temperature melt dynamics. J Non-Cryst Solids 471:120–127

[8] Botta WJ, Berger JE, Kiminami CS, Roche V, Nogueira RP, Bolfarini C (2014) Corrosion resistance of Fe–based amorphous alloys. J Alloy Compd 586:S105–S110

[9] Chu ZH, Wei FS, Zheng XW, Zhang CY, Yang Y (2019) Microstructure and properties of TiN/Fe–based amorphous composite coatings fabricated by reactive plasma spraying. J Alloy Compd 785:206–213

[10] Avar B, Panigrahi M, Soguksu AK, Rajendrachari S, Gundes A (2022) Photocatalytic activity of soft magnetic Fe80−x-CoxZr10Si10 (x = 0, 40, and 80) nanocrystalline melt-spun ribbons. Topics Catal. https://doi.org/10.1007/s11244-022-01569-7

[11] Inoue A, Takeuchi A (2002) Recent progress in bulk glassy alloys. Mater Transact 43:1892–1906

[12] Kong FL, Chang CT, Inoue A, Shalaan E, Al-Marzouki F (2014) Fe-based amorphous soft magnetic alloys with high saturation magnetization and good bending ductility. J Alloys Compd 615:163–166

[13] Liu XD, Wang JT, Zhu J (1994) Comparison of structure and properties of alloys in amorphous, nanocrystalline and coarse-grained polycrystalline states. J Mater Sci 29:929–933. https://doi.org/10.1007/BF00351411

[14] Lu Y, Huang G, Wang Y, Li H, Qin Z, Lu X (2018) Crack-free Fe-based amorphous coating synthesized by laser cladding. Mater Lett 210:46–50

[15] Suryanarayana C (1999) Mechanical alloying. Pergamon Mater Ser 2:49–85

[16] Avar B, Simsek T, Ozcan S, Chattopadhyay AK, Kalkan B (2021) Structural stability of mechanically alloyed amorphous $(FeCoNi)_{70}Ti_{10}B_{20}$ under high-temperature and high-pressure. J Alloys Compd 860:158528. https://doi.org/10.1016/j.jallcom.2020.158528

[17] Agrawal KM, Ranwa JR, Meena SS, Yusuf SM, Mukhopadhyay NK (2017) The effect of Mn on the structural and magnetic behaviour of Fe–6Si–8B alloy produced by high energy ball Milling. Trans Indian Inst Met 70(6):1431–2143

[18] Pablo Álvarez-Alonso JD, Santos MJ, Pérez CF, Sánchez-Valdes JLS, Llamazares PGo (2013) The substitution effect of chromium on the magnetic properties of $(Fe_{1−x}Cr_x)_{80-}Si_6B_{14}$ metallic glasses ($0.02 \leq x \leq 0.14$). J Magn Magn Mater 347:75–78. https://doi.org/10.1016/j.jmmm.2013.07.048

[19] Yapp R, Watts BE, Leccabue F (2000) Characterisation of amorphous Fe–Cr–Si–B alloys. J Magn Magn Mater 215–216(2):300–302

[20] Xu DD, Zhou BL, Wang QQ, Zhou J, Yang WM, Yuan CC, Xue L, Fan XD, Ma LQ, Shen BL (2018) Effects of Cr addition on thermal stability, soft magnetic properties and corrosion resistance of FeSiB amorphous alloys. Corros Sci 138:20–27

[21] Avar B, Chattopadhyay AK, Simsek T, Simse T, Ozcan S, Kalkan B (2022) Synthesis and characterization of amorphous-nanocrystalline $Fe_{70}Cr_{10}Nb_{10}B_{10}$ powders by mechanical alloying. Appl Phys A 128:537. https://doi.org/10.1007/s00339-022-05680-0

[22] Wang JC, Jia Z, Liang SX, Qin P, Zhang WC, Wang WM, SercombeZhang TBLC (2018) $Fe_{73.5}Si_{13.5}B_9Cu_1Nb_3$ metallic glass: rapid activation of peroxymonosulfate towards ultrafast Eosin Y degradation. Mater Des 140:73–84

[23] Zhang CQ, Zhu ZW, Zhang HF, Hu ZQ (2012) On the decolorization property of Fe-Mo-Si-B alloys with different structures. J Non-Cryst Solids 358:61–64

[24] Xiang-Cheng Sun J, Reyes-Gasga NN, Sun WS (2002) Nanocrystallization process and ferromagnetic properties of amorphous $(Fe_{0.99}Mo_{0.01})_{78}Si_9B_{13}$ ribbons. Curr Appl Phys 2(3):187–191. https://doi.org/10.1016/S1567-1739(01)00109-2

[25] Yanhu Li X, Jia YXu, Chang C, Zhang W (2017) Soft magnetic Fe-Si-B-Cu nanocrystalline alloys with high Cu concentrations. J Alloys Compd 722:859–863

[26] Li Y, Jia X, Zhang W, Zhang Y, Jiao Z (2021) Formation and crystallization behavior of Fe-based amorphous precursors

with pre-existing α-Fe nanoparticles —structure and magnetic properties of high-Cu-content Fe-Si-B-Cu-Nb nanocrystalline alloys. J Mater Sci Technol 65:171–181

[27] Zhou J, Kong D (2020) Effects of Al and Ti additions on corrosive–wear and electrochemical behaviors of laser cladded FeSiB coatings. Opt Laser Techno 124:105958. https://doi.org/10.1016/j.optlastec.2019.105958

[28] Lutterotti L (2000) Maud: a Rietveld analysis program designed for the internet and experiment integration. Acta Crystallogr A Found Crystallogr 56(s1):s54–s54. https://doi.org/10.1107/S0108767300021954

[29] Žák T, Jiraskova Y (2006) CONFIT: Mössbauer spectra fitting program. Surf Interface Anal 38(4):710–714

[30] Avar B, Ozcan S (2015) Characterization and amorphous phase formation of mechanically alloyed $Co_{60}Fe_5Ni_5Ti_{25}B_5$ powders. J Alloys Compd 650:53–58

[31] Taghvaei AH, Stoica M, Vaughan G, Ghaffari M, Maleksaeedi S, Janghorban K (2012) Microstructural characterization and amorphous phase formation in $Co_{40}Fe_{22}Ta_8B_{30}$ powders produced by mechanical alloying. J Alloys Compd 512:85–93

[32] Amini R, Shokrollahi H, Salahinejad E, Hadianfard MJ, Marasi M, Sritharan T (2009) Microstructural, thermal and magnetic properties of amorphous/nanocrystalline FeCrMnN alloys prepared by mechanical alloying and subsequent heat treatment. J Alloys Compd 480(2):617–624

[33] Besmel R, Ghaffari M, Shokrollahi H, Chitsazan B, Karimi L (2011) Influence of milling time on the structural, microstructural and magnetic properties of mechanically alloyed $Ni_{58}Fe_{12}Zr_{10}Hf_{10}B_{10}$ nanostructured/amorphous powders. J Magn Magn Mater 323(22):2727–2733

[34] Nowroozi MA, Shokrollahi H (2013) Magnetic and structural properties of amorphous/nanocrystalline $Fe_{42}Ni_{28}Zr_8$-$Ta_2B_{10}C_{10}$ soft magnetic alloy produced by mechanical alloying. Adv Powder Technol 24(6):1100–1108

[35] Sharma S, Suryanarayana C (2008) Effect of Nb on the glass-forming ability of the mechanically alloyed Fe–Ni–Zr–B alloys. Scr Mater 58:508–511

[36] Wang Y, Lu Q, Xiao L, Shi Z (2014) Laser cladding Fe-Cr-Si-P amorphous coatings on 304L stainless. Rare Met Mater Eng 43:274–277

[37] Guérault H, Greneche JM (2000) "Microstructural modelling of nanostructured fluoride powders prepared by mechanical milling. J Condens Matter Phys 12(22):4791–4798

[38] Hasegawa R (ed) (1983) Glassy metals: magnetic, chemical and structural properties (p. 184). CRC Press, Boca Raton

[39] Avar B (2016) Structural, thermal and magnetic characterization of nanocrystalline $Co_{65}Ti_{25}W_5B_5$ powders prepared by mechanical alloying. J Non-Cryst Solids 432:246–253

[40] Yang C, Wei T, Zeng J, Liu LH, Qu SG, Li YY (2012) Microstructure evolution and thermal properties in FeMoPCB alloy during mechanical alloying. J Non-Cryst Solids 358(12–13):1459–1464. https://doi.org/10.1016/j.jnoncrysol.2012.03.024

[41] Nasibi S, Shokrollahi H, Karimi L, Janghorban K (2012) Investigation of structural, microstructural and magnetic properties of mechanically alloyed amorphous/nanocrystalline $Fe_{32.5}Co_{32.5}Nb_{35}$ powders. Powder Technol 228:404–409

[42] Wang J, Zheng Z, Xu J, Wang Y (2014) Microstructure and magnetic properties of mechanically alloyed FeSiBAlNi (Nb) high entropy alloys. J Magn Magn Mater 355:58–64

[43] Daryoush S, Mirzadeh H, Ataie A (2022) Amorphization, mechano-crystallization, and crystallization kinetics of mechanically alloyed AlFeCuZnTi high-entropy alloys. Mater Lett 307(15):131098. https://doi.org/10.1016/j.matlet.2021.131098

[44] Wei R, Sun H, Chen C, Han Z, Li F (2017) Effect of cooling rate on the phase structure and magnetic properties of $Fe_{26.7}Co_{28.5}Ni_{28.5}Si_{4.6}B_{8.7}P_3$ high entropy alloy. J Magn Magn Mater 435:184–186

[45] Xu J, Shang C, Ge W, Jia H, Liaw PK, Wang Y (2016) Effects of elemental addition on the microstructure, thermal stability, and magnetic properties of the mechanically alloyed FeSiBAlNi high entropy alloys. Adv Powder Technol 27:1418–1426

[46] Minor W, Schönfeld B, Lebech B, Buras B, Dmowski W (1987) Crystallization of Fe-Si-B metallic glasses studied by X-ray synchrotron radiation. J Mater Sci 22:4144–4152. https://doi.org/10.1007/BF01133371

[47] Neamţu BV, Marinca TF, Chicinaş I, Isnard O, Popa F, Pǎşcuţǎ P (2014) Preparation and soft magnetic properties of spark plasma sintered compacts based on Fe–Si–B glassy powder. J alloys Compd 600:1–7

[48] Inoue A, Gook JS (1995) Fe-based ferromagnetic glassy alloys with wide super cooled liquid region. Mater Trans JIM 36:1180–1183

[49] Inoue A, Gook JS (1995) Multi component Fe-based glassy alloys with wide super cooled liquid region before crystallization. Mater Trans JIM 36(10):1282–1285

[50] Chang HW, Huang YC, Chang CW, Chiu CH, Chang WC (2008) Glass formability and soft magnetic properties of bulk Y-Fe–B–Ti metals. J Alloys Compd 462(1–2):68–72

[51] Movahedi B, Enayati MH, Wong CC (2010) Structural and thermal Behavior of Fe-Cr-Mo-P-B-C-Si Amorphous and Nanocrystalline HVOF Coatings. J Therm Spray Technol 19(5):1093–1099

[52] Suryanarayana C, Inoue A (2010) Bulk metallic glass. CRC Press, Boca Raton

[53] Vyazovkin S (2020) Kissinger method in kinetics of materials: things to beware and be aware of. Molecules 25:2813. https://doi.org/10.3390/molecules25122813

[54] Parra C, Perea D, Bolivar FJ (2020) Effect of cobalt content on non-isothermal crystallization kinetics of Fe-based amorphous alloys. RevistaFacultad de Ingeniería Universidad de Antioquia 95:44–52

[55] Suñol JJ, Clavaguera-Mora MT, Clavaguera N (2002) Thermally activated crystallization of two FeNiPSi alloys. J Therm Anal Calorim 70:173–179

[56] Malow TR, Koch CC (1997) Grain growth in nanocrystalline iron prepared by mechanical attrition. Acta Mater 45:2177–2186. https://doi.org/10.1016/S1359-6454(96)00300-X

[57] Xiao Z, Luo F, Tang C, Chen L, Ngai TL (2014) Study of amorphous phase in $Fe_{100-x}(NbTiTa)_x$ alloys synthesized by mechanical alloying and its effect on the crystallization phenomenon. J Non-Cryst Solids 385:117–123

[58] Liu YJ, Chang ITH, Lees MR (2001) Thermodynamic and magnetic properties of multicomponent (Fe, Ni)70Zr10B20 amorphous alloy powders made by mechanical alloying. Mater Sci Eng A 304–306:992–996

[59] Herzer G (2013) Modern soft magnets: amorphous and nanocrystalline materials. Acta Mater 61:718–734

[60] Liu J, Schliep K, He S, Ma B, Jing Y, Flannigan DJ, Wang J (2018) Iron nanoparticles with tunable tetragonal structure and magnetic properties. Phys Rev Mater 2:054415. https://doi.org/10.1103/PHYSREVMATERIALS.2.054415

[61] Nowroozi MA, Shokrollahi H (2013) Magnetic and structural properties of amorphous/nanocrystalline $Fe_{42}Ni_{28}Zr_8Ta_2B_{10}C_{10}$ soft magnetic alloy produced by mechanical alloying. J Magn Magn Mater 335:53–58

[62] Taghvaei AH, Stoica M, Khoshkhoo MS, Thomas J, Vaughan G, Ghaffari M, Janghorban K, Eckert J (2012) Microstructure and magnetic properties of amorphous/nanocrystalline $Co_{40}Fe_{22}Ta_8B_{30}$ alloy produced by mechanical alloying. Mater Chem Phys 134:1214–1224

[63] Wang J, Zheng Z, Xu J, Wang Y (2014) Effects of Al and Si addition on the structure and properties of CoFeNi equal atomic ratio alloy. J Magn Magn Mater 355:58–64

[64] Nowroozi MA, Shokrollahi H (2013) Microstructural evolution and amorphous phase formation of $Fe_{42}Ni_{28}Zr_8Ta_2B_{10}C_{10}$ alloy produced by mechanical alloying Adv. Powder Technol 24:1100–1108

[65] Alleg S, Kartout S, Ibrir M, Azzaza S, Fenineche NE, Sunol JJ (2013) Magnetic, structural and thermal properties of the Finemet-type powders prepared by mechanical alloying. J Phys Chem Solids 74:550–557

[66] Li YH, Jia XJ, Xu YQ, Chang CT, Xie GQ (2017) Zhang W Soft magnetic Fe-Si-B-Cu nanocrystalline alloys with high Cu concentrations. J Alloy Compd 722:859–863

[67] Jia XJ, Li YH, Wu LC, Zhang Y, Xie L, Zhang W (2019) The role of Cu content on structure and magnetic properties of Fe-Si-B-P-Cu nanocrystalline alloys. J Mater Sci 54:4400–4408. https://doi.org/10.1007/s10853-020-05404-w

[68] Hono K, Ping DH, Ohnuma M, Onodera H (1999) Cu clustering and Si partitioning in the early crystallization stage of an Fe73 5Si13 5B9Nb3Cu1 amorphous alloy. Acta Mater 47(3):997–1006